Gold nanorod gradient surfaces

Applied Surface Science 729 (2026) 166104

Contents lists available at ScienceDirect

Applied Surface Science

journal homepage: www.elsevier.com/locate/apsusc

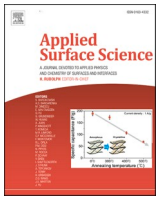

Full Length Article

Gold nanorod gradient surfaces

Maja Lidström Uusitalo [a], Michal Strach [b], Mats Hulander [a], Martin Andersson [a,*]

[a] Department of Chemistry and Chemical Engineering, Chalmers University of Technology, SE-412 96 Gothenburg, Sweden
[b] Chalmers Materials Analysis Laboratory, Chalmers University of Technology, SE-412 96 Gothenburg, Sweden

ARTICLE INFO

Keywords:
Gold nanorods
Nanoparticle gradient surface
Thermoplasmonics

ABSTRACT

Materials based on solid-supported nanoparticles are used in a range of applications, spanning from catalysis to sensing. Controlling the inter-nanoparticle distance is essential in property optimization of these materials. To achieve such control, nanoparticle gradient surfaces, where nanoparticles are attached in a number density gradient on the support, show great promise. This study presents a tunable method for the preparation of gold nanorod gradient surfaces, exploiting nanoparticle adsorption kinetics to control the surface coverage. The method involves immersing a mercapto silane-functionalized substrate in a gold nanorod suspension, which is then withdrawn at a fixed rate. We show that the gradient dynamics can be tuned by changing the withdrawal rate, and that the gradients exhibit a linear increase in surface coverage along the distance of the support. The changes in optical properties and influence of plasmon coupling with the surface coverage of gold nanorods were evaluated using extinction spectroscopy. Additionally, by assessing the photothermal properties of the gradients upon irradiation with a near-infrared laser, through thermal imaging and *in situ* X-ray diffraction, we show that a temperature gradient is achieved, correlating with the increased surface coverage of gold nanorods.

1. Introduction

In recent decades, nanoparticles have attracted great research interest owing to their unique optical, catalytic, and mechanical properties. To harness these properties, it is often necessary to immobilize the nanoparticles on the surface of a solid support material. Solid-supported nanoparticles have been employed in a range of applications, including heterogeneous catalysis [1], sensing [2], investigations of biological phenomena such as cell adhesion [3], and in the development of antibacterial or antifouling materials [4]. These materials can be made using top-down approaches, for example electron beam lithography [5], allowing for high spatial precision and reproducibility, or bottom-up approaches, for example by assembling pre-formed nanoparticles [6,7], facilitating precise control of attachment density as well as nanoparticle size and shape. The properties of materials based on solid-supported nanoparticles are determined not only by the nanoparticles' intrinsic properties but also by their arrangement on the support and the interparticle interactions. Consequently, the ability to control the nanoparticle surface-attachment is a key factor in the development and optimization of such materials.

Nanoparticle gradient surfaces, in which the nanoparticles are attached in a number density gradient along the support, hold great potential for the development of materials based on solid-supported nanoparticles. Such gradients not only enable accurate evaluation and optimization of the material's properties but also enable screening or combinatorial studies on a single sample. A range of methodologies have been developed to manufacture nanoparticle gradient surfaces. One common approach is the generation of a chemical gradient on the surface to which the nanoparticles are subsequently attached [8,9]. Other strategies include bipolar electrodeposition [10], magnetolithography [11], and controlling chemisorption to the support by creating a gradient in ionic strength in the nanoparticle suspension [12]. An alternative methodology for creating a nanoparticle gradient relies on utilizing the kinetics of nanoparticles adsorption through dip-coating [13]. In this case, the exposure time of the surface to the nanoparticle suspension determines the number of adsorbed particles, providing a tunable approach to gradient formation.

In the development of nanoparticle gradient surfaces, gold nanoparticles are a popular choice owing to their tunable optical properties, high photothermal conversion efficiency [14], and catalytic activity [1]. Furthermore, their relatively low toxicity potential [15–17], makes them suitable for applications involving biological systems. Previous work on gold nanoparticle gradient surfaces have primarily utilized spherical particles [8–10,12], whereas in this study, we present a

* Corresponding author at: Department of Chemistry and Chemical Engineering, Chalmers University of Technology, SE-412 96 Gothenburg, Sweden.
E-mail address: martin.andersson@chalmers.se (M. Andersson).

https://doi.org/10.1016/j.apsusc.2026.166104
Received 19 November 2025; Received in revised form 12 January 2026; Accepted 26 January 2026
Available online 27 January 2026

method for the preparation of nanoparticle gradient surfaces using anisotropic gold nanoparticles, specifically gold nanorods. Gold nanorods exhibit several benefits compared to their spherical counterpart, including higher sensitivity in optical sensing [14], and the ability to tune the plasmon resonance frequency to the near-infrared (NIR) region known as the biological window, where tissue penetration is maximized [18].

In this study, gold nanorod gradient surfaces were prepared utilizing nanoparticle adsorption kinetics, where gradual withdrawal of the nanoparticle suspension from the substrate controlled the surface coverage of nanorods. We evaluated how the gradient dynamics were influenced by the withdrawal rate and characterized the gradients' optical properties using extinction spectroscopy. Finally, the photothermal response under NIR laser irradiation was evaluated using thermal imaging and *in situ* X-ray diffraction, to assess how the nanoparticles' heating depends on surface density.

2. Results and discussion

2.1. Gold nanorod gradient surface preparation

Gold nanorod gradient surfaces were prepared on fused silica substrates (9 mm × 20 mm × 0.3 mm) functionalized with (3-mercaptopropyl)trimethoxysilane (3-MPS), enabling the gold nanorods to attach via thiol-gold bonding. The functionalized substrates were immersed vertically in a gold nanorod suspension, and immediately after immersion the withdrawal of the suspension through a syringe needle connected to a programmable syringe pump was initiated. A schematic illustration of the gradient preparation setup is shown in Fig. 1A, and photos of the setup are included in Fig. 1B and Fig. S3. This process yields a gold nanorod gradient surface where the surface coverage of particles increases from the top to the bottom of the substrate. By varying the withdrawal rate, the gradient dynamics could be tuned, with higher withdrawal rates resulting in an overall lower particle coverage.

2.2. Gold nanorod gradient surface characterization

In this study, two different withdrawal rates were employed, 0.15 mm min^{-1} and 0.30 mm min^{-1}. Scanning electron microscopy (SEM) micrographs were acquired every millimeter along the lengths of the gradients to evaluate the gold nanorod surface coverage as a function of distance. Composite images of one 0.15 mm min^{-1} and one 0.30 mm min^{-1} gradient are shown in Fig. 2A and B, respectively. SEM analysis revealed an increase in the number density of gold nanorods from the top part of the substrate (left in Fig. 2), which was exposed to the nanorod suspension for the shortest amount of time, to the bottom part (right in Fig. 2), which was exposed for the longest time. At the low surface coverage end of the gradients, the gold nanorods were attached almost solely as individual particles. As the surface coverage increased, some clustering of the gold nanorods could be observed, most clearly shown in the right part of the 0.15 mm min^{-1} composite image in Fig. 2A.

The surface coverage of gold nanorods was determined through image analysis of the SEM micrographs, expressed as the projected area covered by particles (in percent). The average surface coverage of four independent samples (n = 4) of the 0.15 mm min^{-1} and the 0.30 mm min^{-1} gradients as a function of distance along the support are shown in Fig. 2C. Error bars indicate the standard deviation between the four samples, and the dashed lines the linear regressions fitted to the data. For the 0.15 mm min^{-1} gradients, the surface coverage ranged from 3% to 11% and exhibited a linear increase with distance along the gradient. A similar trend could be observed for the 0.30 mm min^{-1} gradients, where the surface coverage ranged from 2% to 9%. It is worth noting that the surface coverage at the far end of the 0.30 mm min^{-1} gradients (around 19 mm distance) appears to deviate slightly from the linear trend, obtaining a higher coverage than expected. This deviation is likely due to edge effects, where the gold nanorod suspension forms droplets at the bottom edge of the substrates during withdrawal, causing these parts to be exposed to the suspension for a prolonged time. The differences between the 0.15 mm min^{-1} and 0.30 mm min^{-1} samples demonstrate that the gradient dynamics can be tuned by adjusting the withdrawal rate of the gold nanorod suspension, providing ease of control over the overall surface coverage of gold nanorods.

The surface coverage could also be related to the scattering intensity of the gold (200) peak in XRD patterns collected along the gradient. Diffraction patterns were acquired every 3 mm over the 9–18 mm range of a 0.15 mm min^{-1} gradient, using identical exposure settings (unprocessed XRD patterns shown in Fig. S4). The X-ray beam size was set to 2 mm × 2 mm, and with the sample tilted at 22°, this corresponds to an illuminated area of approximately 2 mm (along the length) × 5.3 mm (along the width). The peaks were fitted and the intensity at each measured area is plotted in Fig. 2D as a function of the position. The

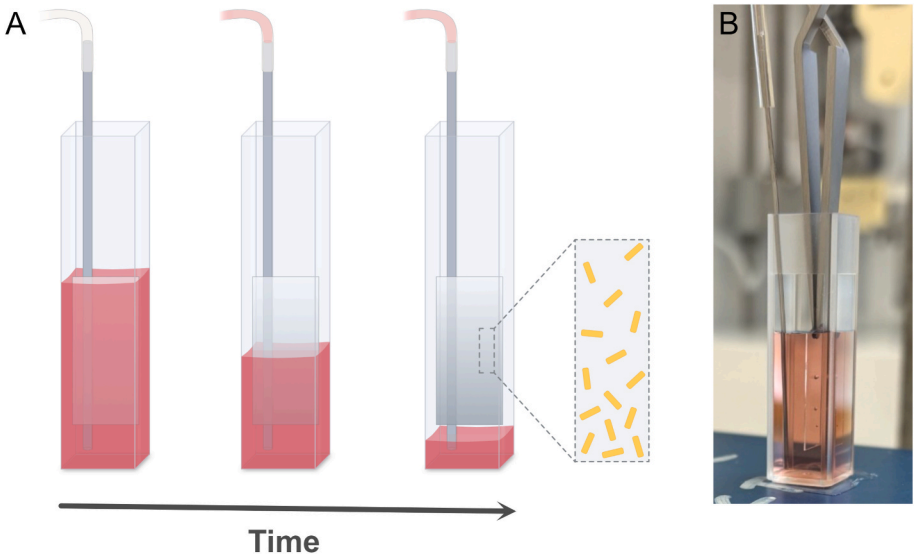

Fig. 1. (A) A schematic illustration of the gold nanorod gradient surface preparation setup. A fused silica substrate functionalized with (3-mercaptopropyl)trimethoxysilane is immersed vertically in a gold nanorod suspension, which is withdrawn at a set rate through a syringe needle connected to a programmable syringe pump. This process results in a surface coverage of gold nanorods that increases from the top to the bottom of the substrate. (B) A photo of the gradient surface preparation setup at the start of the process (t = 0).

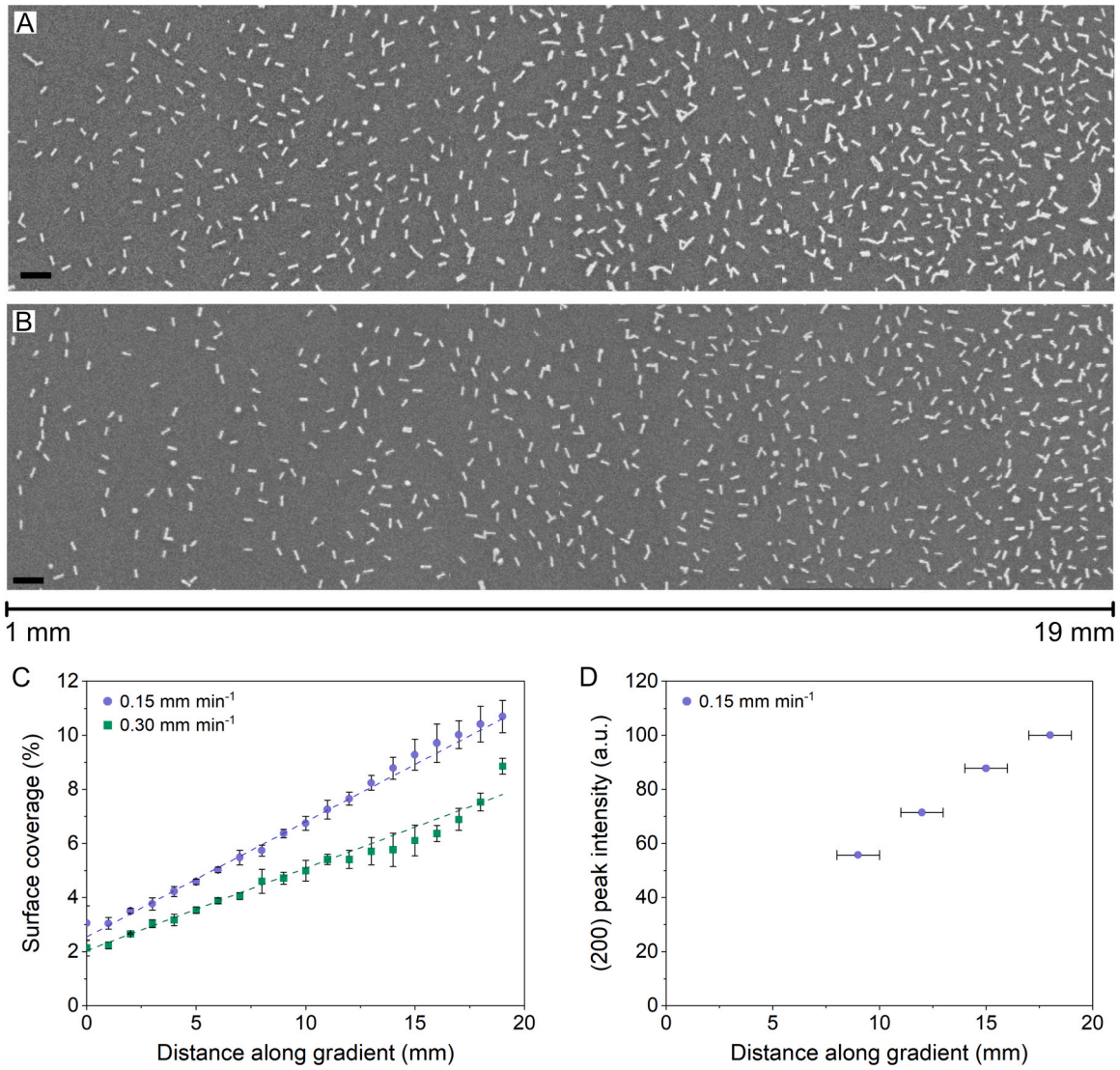

Fig. 2. Composite images from multiple SEM micrographs acquired every 1 mm along the length of the gradients for (A) one gradient prepared with a withdrawal rate 0.15 mm min^{-1}, and (B) one gradient prepared with a withdrawal rate of 0.30 mm min^{-1}. The scale bars are 200 nm. (C) Surface coverage of gold nanorods (projected area) in percent as a function of the distance along the gradient in millimeters for the 0.15 mm min^{-1} and 0.30 mm min^{-1} gradients (n = 4). Error bars indicate the standard deviation, and the dashed lines the linear regressions fitted to the experimental data, $y = 0.424x + 2.55$ $(R^2 = 0.995)$ for 0.15 mm min^{-1} and $y = 0.304x + 2.04$ $(R^2 = 0.986)$ for 0.30 mm min^{-1}. (D) (200) diffraction peak intensity as a function of distance along a 0.15 mm min^{-1} gradient, with horizontal bars indicating the 2 mm region probed by the X-ray beam.

(200) peak intensity increased linearly along the distance of the gradient, in agreement with the increase in surface coverage as determined by image analysis of SEM micrographs.

The optical properties of the gold nanorod gradient surfaces were characterized by measuring extinction spectra in air at 2 mm intervals along the samples. Representative spectra for one 0.15 mm min^{-1} gradient are shown in Fig. 3A, and of a 0.30 mm min^{-1} gradient in Fig. 3B. In the extinction spectra, the gold nanorods' two characteristic localized surface plasmon resonance peaks can be observed. The longitudinal peak centered around 800 nm increased in extinction intensity along the length of the gradient for both withdrawal rates. The longitudinal peak intensity, determined as the average extinction between 800–820 nm, as a function of surface coverage is shown in Fig. 3C and D for the 0.15 mm min^{-1} and 0.30 mm min^{-1} sample, respectively. In both cases, the peak intensity exhibited an approximately linear increase with nanorod surface coverage.

A shoulder on the longitudinal peak was observed further into the NIR region, around 1000 nm, as the surface coverage of gold nanorods increased. The shoulder intensity, determined as the average extinction between 990–1010 nm, as a function of surface coverage is shown in Fig. 3C and D for the 0.15 mm min^{-1} and 0.30 mm min^{-1} sample, respectively. An increase in shoulder extinction intensity was observed at surface coverages above 8%. The appearance of this shoulder, which accompanies the higher surface coverage of gold nanorods, is likely due to plasmon coupling between neighboring nanorods. As the surface coverage increases, the interparticle distances decrease and the amount of clustered nanorods increases, inducing plasmon coupling between the particles which can explain the observed changes in optical properties [19]. These gold nanorod surface gradients could thus provide a platform for evaluating the influence of plasmon coupling as a function of nanoparticle surface density.

2.3. Gold nanorod adsorption kinetics

To evaluate the gold nanorod adsorption kinetics during the gradient surface preparation, the surface coverage was analyzed as a function of

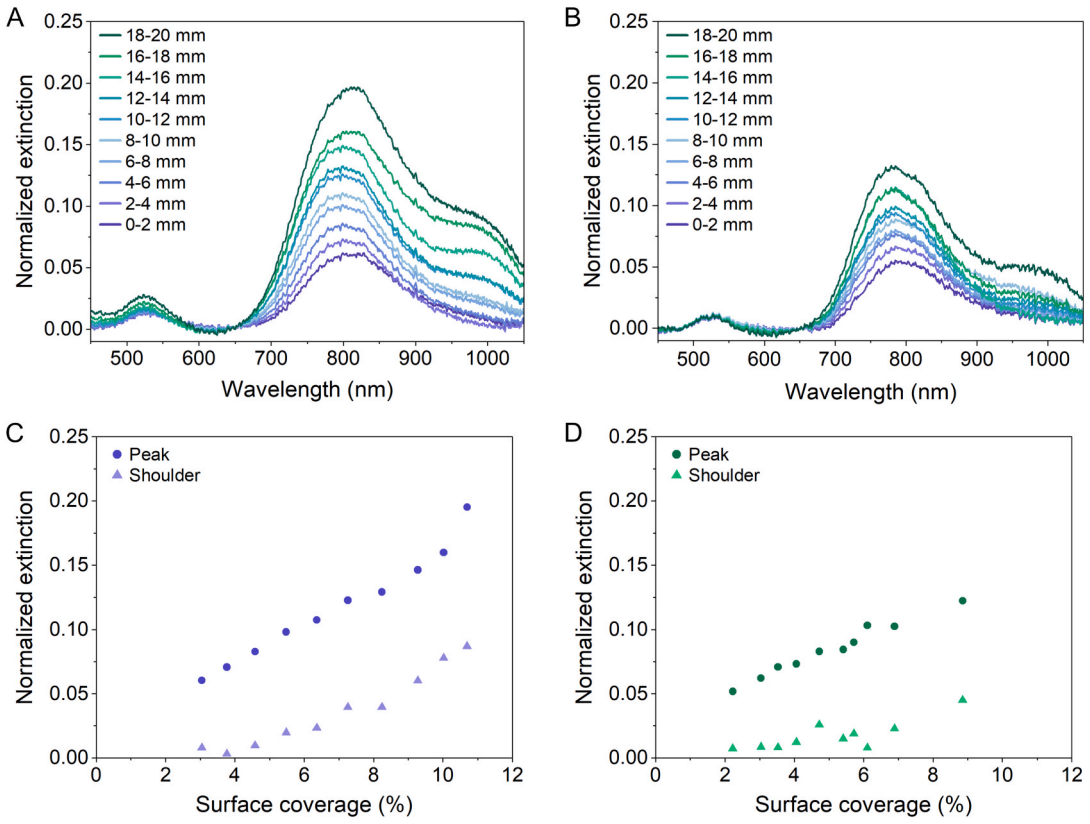

Fig. 3. Normalized extinction spectra recorded at 2 mm intervals along the gradient for (A) a 0.15 mm min^{-1} sample, and (B) a 0.30 mm min^{-1} sample. Extinction peak intensity (average extinction between 800–820 nm) and shoulder intensity (average extinction between 990–1010 nm) as a function of the surface coverage of gold nanorods for (C) a 0.15 mm min^{-1} sample, and (D) a 0.30 mm min^{-1} sample.

exposure time in the gold nanorod suspension. The exposure time at each position along the gradient was estimated from the withdrawal rates and correlated with the surface coverage determined from SEM micrographs (Fig. 2C). The surface coverage as a function of time for both the 0.15 mm min^{-1} and the 0.30 mm min^{-1} gradients is shown in Fig. 4A. For comparison, the surface coverage evolution for diffusion-limited, irreversible adsorption of gold nanorods to a planar surface from an infinite volume was modelled (details in the Experimental Section) and is also included in Fig. 4A.

The diffusion-limited adsorption model assumes a system without convective mixing, where the particle transport from the bulk to the substrate surface is the rate-limiting step in the adsorption process. As shown in Fig. 4A, the modelled diffusion-limited adsorption yields a slower increase in surface coverage over time ($\propto t^{1/2}$) compared to the experimental data. In the gradient preparation setup, no mixing of the gold nanorod suspension occurs, and thus most of the substrate will be immersed in a suspension with low levels of convective mixing, where the gold nanorod adsorption should roughly follow the diffusion-limited process. However, as the gold nanorod suspension is withdrawn from the substrate, a liquid meniscus will form along the substrate at the liquid–air interface, as illustrated in Fig. 4B. In this region, an increased flux of nanoparticles to the substrate can occur, like the phenomena

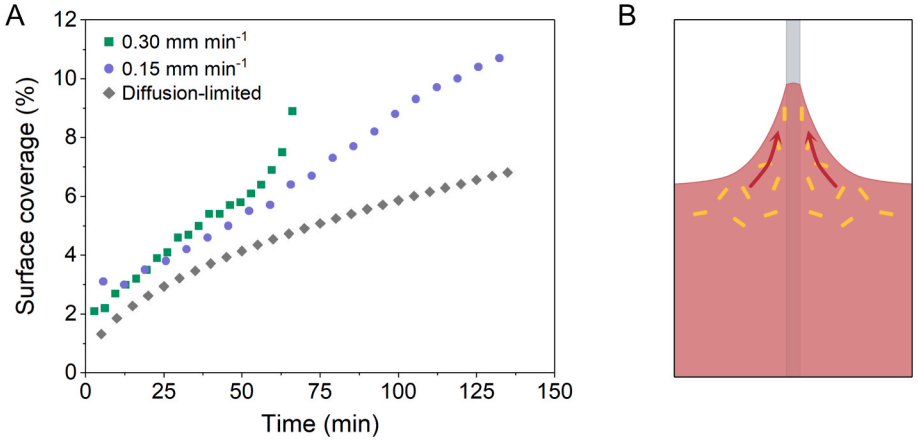

Fig. 4. (A) Surface coverage as a function of exposure time in the gold nanorod suspension for the 0.15 mm min^{-1} and 0.30 mm min^{-1} gradients, as well as the modelled surface coverage evolution for diffusion-limited, irreversible adsorption of gold nanorods to a planar surface from an infinite volume. (B) Schematic illustration of the liquid meniscus formed along the substrate as the gold nanorod suspension is withdrawn.

utilized in convective self-assembly [20]. As the liquid front recedes along the substrate, the local flux of gold nanorods would increase, thereby enhancing the adsorption rate. This effect explains why the experimental surface coverage increases more steeply with time compared to the modelled diffusion-limited adsorption.

The experimental data shows an approximately linear dependence on exposure time ($\propto t$), in contrast to the $t^{1/2}$ increase expected for a diffusion-limited adsorption process. This observation indicates that the gold nanorod adsorption during the gradient surface manufacturing is a reaction-limited process, wherein the binding of the particles to the substrate is rate determining. A reaction-limited adsorption process is reasonable given the system of CTAB-stabilized gold nanorods adsorbing onto a 3-MPS functionalized silica substrate. The attachment of the gold nanorods to the substrate is likely influenced by the density of the 3-MPS layer, and by the orientation of the nanorods as they approach the surface. It is generally accepted that the CTAB layer is less dense at the gold nanorod ends due to crystallographic habits and high curvature [21], making the ends of the particles more easily functionalized. Therefore, a rod orientation with the end facing the substrate is likely more favorable for binding to the 3-MPS layer. These restrictions on nanorod surface binding, combined with the high particle flux in the liquid meniscus and the observed linear increase in surface coverage over time, support the conclusion that adsorption in the gradient preparation is reaction-limited. It is worth noting that in the prepared gradient samples, the majority of the nanorods are oriented with the long axis towards the support and not the ends, as can be observed in the SEM micrographs in Fig. 2A and B. It is probable that the final orientation of the nanorods is obtained upon drying, wherein the capillary forces cause the nanorods to reorient into lying flat along the support, minimizing the surface energy.

2.4. Evaluation of photothermal properties

The photothermal properties of the gold nanorod gradient surfaces were evaluated by monitoring the heating of the samples during irradiation with an 808 nm NIR laser at an intensity of 0.6 W cm^{-2}. Heating was monitored *in situ* using a thermal imager at 10, 30, and 50 s. The heating profiles of a 0.15 mm min^{-1} gradient are shown in the top row of Fig. 5 and the heating of a 0.30 mm min^{-1} gradient in the bottom row. For clarity, the area corresponding to the samples have been outlined in black. In both cases, a temperature increase was observed, caused by the photothermal heating of the gold nanorods upon irradiation with the NIR laser. Notably, a gradient in temperature developed along each sample, corresponding to the increase in surface coverage of gold nanorods. After 50 s irradiation, the temperature difference between the low and high surface coverage part of the gradients was 2–4 °C. Furthermore, the 0.15 mm min^{-1} gradient reached an overall higher temperature compared to the 0.30 mm min^{-1} gradient, reflecting the difference in surface coverage between the two sample types.

The photothermal properties of the 0.15 mm min^{-1} gradient were also evaluated by *in situ* XRD measurements under NIR laser irradiation. A series of irradiation experiments were performed at four different positions along the gradient: 9, 12, 15 and 18 mm. Areas with lower coverage could not be probed due to limited intensity of the (200) diffraction peak. The X-ray beam size was 2 mm × 2 mm, and the NIR laser beam spot had a diameter of 2 mm, thus at each position a range of ±1 mm along the length of the gradient was probed. A photo of the experimental setup is included in Fig. S5. At each position, XRD patterns were acquired at room temperature and under consecutive irradiation at 28, 56, 84, and 112 W cm^{-2}. The (200) peak shifts were used to estimate the temperature of the gold nanorods, according to a previously described protocol [22]. Using the known surface coverage at each position along the 0.15 mm min^{-1} gradient (Fig. 2C), we established a relationship between the temperature of the gold nanorods as a function of the surface coverage, at the four different laser intensities, shown in Fig. 6. The unprocessed diffraction patterns are included in Fig. S6. An increase in the temperature of the gold nanorods along the gradient was observed, demonstrating how the nanoparticle heating is influenced by the surface coverage. At 56 W cm^{-2}, the gold nanorods at the highest probed surface coverage (~10%, 18 mm distance) reached around 150 °C, while those at the lowest coverage (~6%, 9 mm distance) reached 100 °C, thus giving a temperature difference of 50 °C.

As observed in our previous work, gold nanorods undergo irreversible morphological changes at elevated temperatures, with an onset

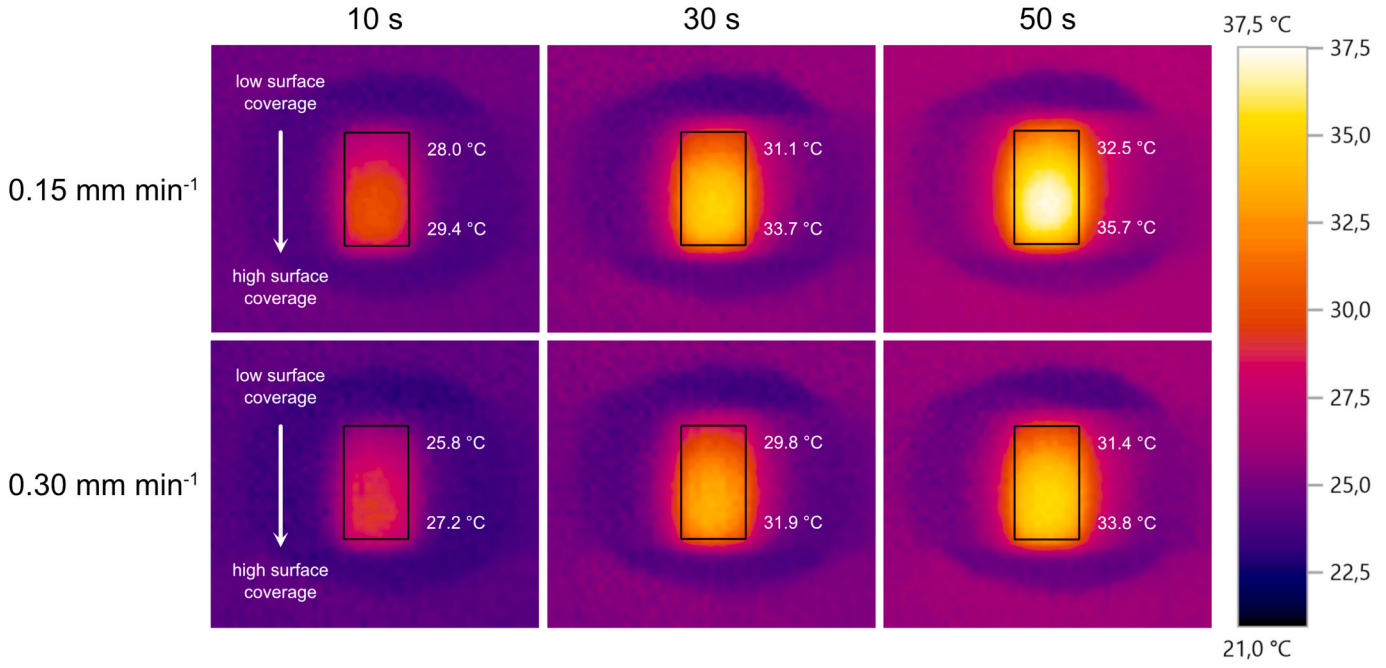

Fig. 5. Thermal imaging of gold nanorod gradient surfaces prepared at 0.15 mm min^{-1} (top) and 0.30 mm min^{-1} (bottom) during irradiation with NIR light (808 nm) at an intensity of 0.6 W cm^{-2}. The black rectangular outlines indicate the gold nanorod gradient surfaces, oriented so that the surface coverage increases from top to bottom.

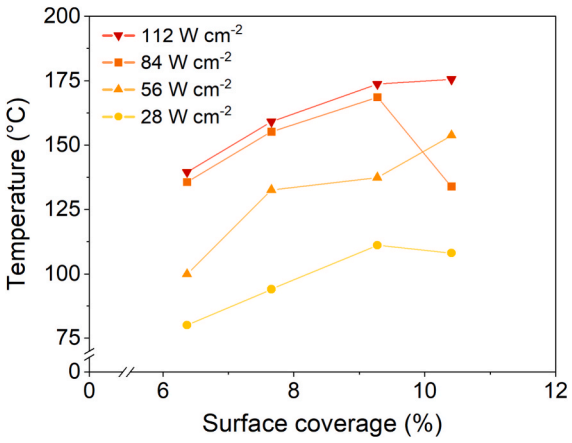

Fig. 6. The temperature of the gold nanorods as a function of the surface coverage of a 0.15 mm min^{-1} gradient, at four different NIR laser intensities, as determined by *in situ* XRD.

around 120 °C [22]. These changes include a reduction in aspect ratio of the gold nanorods and the coalescence of clustered particles, resulting in a blue-shift of the longitudinal plasmon resonance frequency, as shown by post-experiment SEM and extinction spectroscopy (Fig. S7). Since regions with higher surface coverage of gold nanorods reach a higher temperature and contain more clustered particles, the morphological changes are most prominent here, resulting in larger blue-shifts. These morphological changes also manifest as an irreversible increase in the (200) peak intensity upon laser irradiation. The increase was 1–2% in low coverage areas and increased to 5–8% in the higher coverage regions (Fig. S8).

Because each spot along the gradient was consecutively irradiated with increasing NIR laser intensity, temperatures above the onset of morphological changes (>120 °C) were already reached during the 56 W cm^{-2} irradiation at all probed areas except the lowest surface coverage (6%). When continuing with the measurements at higher laser intensities, the gold nanorods had thus started to change morphology and their longitudinal resonance peak would gradually blue-shift away from the 808 nm excitation, resulting in less efficient light absorption and thus less efficient heating. The 9% and 10% surface coverage regions reached the highest temperatures early during the irradiation sequence, as such the gold nanorods in these areas would be most affected with the largest blue-shifts, which was validated by the post-experiment characterization (Fig. S7). As the regions with higher surface coverage of gold nanorods are most affected by the morphological changes, this explains the deviations from the expected trend of increasing temperature with surface coverage observed in Fig. 6, where the temperature instead plateaus or decreases.

By evaluating the photothermal heating of the gradients under NIR irradiation using both thermal imaging and *in situ* XRD, we demonstrated that a macroscopic temperature gradient develops across the 20 mm sample, and that the temperature of the gold nanorods increases with increasing surface coverage. The tunable photothermal properties of the gold nanorod gradient surfaces make them a valuable platform for evaluating the plasmonic heating as a function of nanoparticle surface density, which is of particular interest for plasmonic nanoparticle arrays, as they are known to exhibit collective heating effects [22,23].

3. Conclusions

We have developed a method for preparing gold nanorod gradient surfaces by immersing a mercapto silane-functionalized substrate into a gold nanorod suspension and withdrawing the suspension at a fixed rate, thereby using adsorption kinetics to control surface coverage. By comparing two withdrawal rates, we demonstrated that the gradient dynamics can be tuned, with higher rates yielding lower overall nanorod coverage. The fabricated gradients exhibited a linear increase in surface coverage of gold nanorods along the length of the gradients, as confirmed by SEM and XRD. The gradients' optical properties were characterized using extinction spectroscopy, revealing a linear increase in the extinction intensity of the longitudinal plasmon resonance peak with the surface coverage, as well as the emergence of plasmon coupling at higher coverages. Under NIR laser irradiation, the gradients displayed a temperature profile correlating with gold nanorod coverage. *In situ* XRD during NIR irradiation further showed that gold nanorod temperature scaled with surface coverage and that this temperature difference was reflected in the extent of irreversible morphological changes. These gradient surfaces therefore provide a versatile platform for evaluating the influence of plasmon coupling and plasmonic heating as a function of nanorod surface density, with potential for applications in screening or combinatorial studies involving solid-supported gold nanorods.

4. Experimental Section

4.1. Gold nanorod synthesis

Gold nanorods were synthesized according to a previously published protocol, producing nanorods with an average length of 67 nm and an average width of 18 nm [22,24], originally adapted from a seed-mediated synthesis published by Scarabelli *et al.* [25]. Briefly, a gold seed suspension was prepared in a 30 °C water bath by mixing 4.7 ml of 100 mM hexadecyltrimethylammonium bromide (CTAB, Sigma-Aldrich, ≥98%) solution with 25 µl of 50 mM gold(III) chloride ($HAuCl_4$, Sigma-Aldrich, ≥99.9%) solution. Subsequently, 300 µl of 10 mM sodium borohydride (Sigma-Aldrich, 99%) solution was added under strong stirring, and the resulting seed suspension was kept under mild stirring at 30 °C until further use. A growth solution was prepared in a 30 °C water bath by mixing 60 ml of 100 mM CTAB solution with 1.14 ml of 1 M hydrochloric acid (Sigma-Aldrich, ≥37%) solution and 600 µl of 50 mM $HAuCl_4$ solution. Thereafter, 720 µl of 10 mM silver nitrate (Sigma-Aldrich, 99.99%) solution was added, followed by 600 µl of 100 mM ascorbic acid (Sigma-Aldrich, 99%) solution. Lastly, 144 µl of the seed suspension was added to the growth solution, mixed thoroughly, and then left undisturbed for 1 h and 50 min at 30 °C. The synthesized gold nanorods were purified by three repeated centrifugations with redispersion in ultrapure water between each. An absorption spectrum of the synthesized gold nanorods is included in Fig. S2.

4.2. Gold nanorod gradient surface preparation

The gold nanorod gradient surfaces were prepared on 9 mm × 20 mm × 0.3 mm fused silica substrates. The substrates were rinsed in 95% ethanol (Solveco) followed by ultrapure water and then dried in a flow of nitrogen gas. Thereafter, the substrates were cleaned by immersion in nitric acid (Sigma-Aldrich, 65–67%) overnight (18–19 h). After nitric acid immersion, the substrates were thoroughly rinsed in ultrapure water followed by 95% ethanol before being functionalized in a 1 mM solution of (3-mercaptopropyl)trimethoxysilane (3-MPS, Sigma-Aldrich, 95%) in 95% ethanol for 1 h. Lastly, the 3-MPS functionalized substrates were rinsed in 95% ethanol followed by ultrapure water and then immediately used in the gold nanorod gradient preparation. The gold nanorod suspension used in the gradient preparation was prepared by diluting the synthesized gold nanorods with ultrapure water to an absorbance at 400 nm of 0.6, which could be estimated to an approximate gold nanorod concentration of 0.25 nM, using the correlation that an absorbance at 400 nm of 1.2 corresponds to $[Au^0] = 0.5$ mM [25]. The gradients were prepared in standard single-use cuvettes (Brand® UV cuvettes macro) with 10 mm path length. The 3-MPS functionalized substrate was immersed vertically 20 mm into the gold nanorod suspension, ensuring the entire substrate was immersed and an approximately 5 mm gap was left in the bottom of the cuvette. The gold nanorod

suspension was thereafter withdrawn at a fixed rate (0.15 or 0.30 mm min^{-1}) from the bottom of the cuvette through a syringe needle using a programmable syringe pump (Fig. S3). The withdrawal rate thus determined how long the different parts of the substrate were immersed in the gold nanorod suspension, with the top part being immersed for the shortest time. A schematic illustration of the setup is shown in Fig. 1A. In this configuration, both sides of the substrate were exposed to the gold nanorod suspension, and as such, the gold nanorods attached to the backside of the samples were removed by wiping with a damp cotton swab, to enable characterization of a single gold nanorod gradient monolayer. The removal of the gold nanorods from the back of the samples was verified using scanning electron microscopy.

4.3. Scanning electron microscopy

The gold nanorod gradient surfaces were characterized using a Zeiss Ultra 55 scanning electron microscope. The samples were imaged in secondary electron mode with an acceleration voltage of 2.5 kV. Micrographs were taken every 1 mm along the length of the gradient, at three different widths, generating a total of 19 × 3 micrographs per sample. The micrographs were analyzed with respect to the surface coverage of gold nanorods (projected area) using the image analysis software ImageJ.

4.4. Extinction spectroscopy

The optical properties of the gold nanorod gradients were characterized by recording extinction spectra every 2 mm along the samples. The extinction spectra were measured on a home-built microscopy/transmission setup equipped with a halogen lamp (Newport) and a 4× air objective (Olympus, NA 0.1). The transmission was recorded with a photodiode array spectrometer (B&WTEK), and the dark counts were subtracted from the measured intensities. The reference intensity was measured through a bare fused silica substrate. To mount the samples in the microscopy/transmission setup, they were attached to microscopy slides and immersion oil was placed between the back of the samples and the slides to minimize refractive index mismatches. To correct for background variations caused by the differences in thickness of the immersion oil layer, the extinction spectra were baseline corrected to 650 nm, where minimal absorption and scattering by the gold nanorods is expected.

4.5. Gold nanorod adsorption kinetics

The gold nanorod adsorption kinetics during the gradient surface formation was evaluated by estimating the time required to reach a certain surface coverage. Based on the dimensions of the cuvettes used for the gradient preparations, the time required to withdraw the gold nanorod suspension from 1 mm of the sample was determined based on the employed withdrawal rates. This enabled establishing a relationship between the surface coverage and the exposure time in the gold nanorod suspension. For comparison, the time evolution of surface coverage predicted for diffusion-limited adsorption to a planar surface was estimated. In the case of diffusion-limited, irreversible adsorption to a planar surface from an infinite volume, the flux of nanoparticles to the surface can be described by the equation (derived from Smoluchowski) [26]

$$-j(t) = \left(\frac{D}{\pi t}\right)^{1/2} n_b \tag{1}$$

where $-j$ is the particle flux in the direction of the surface, n_b the particle concentration in the bulk (number of particles per unit volume), and D the particles' diffusion coefficient. From Eq. (1), the surface concentration of particles, Γ (m^{-2}), can be determined as [26]

$$\Gamma(t) = 2\left(\frac{Dt}{\pi}\right)^{1/2} n_b \tag{2}$$

Lastly, the surface coverage, θ, can be determined by multiplying Γ with the projected area a of a particle, which for a gold nanorod can be estimated as a rectangle.

$$\theta(t) = \Gamma(t)a \tag{3}$$

To evaluate the diffusion-limited adsorption, the gold nanorods translational diffusion coefficient was estimated from [27]

$$D_t = \frac{k_B T}{3\pi\eta_0 L}(\ln p + \nu) \tag{4}$$

Where k_BT is the Boltzmann factor, η_0 the viscosity of the medium, p the aspect ratio of a cylinder of length L and diameter d ($p = L/d$), and ν an end-effect correction, which is a function of p, described by [27]

$$\nu = 0.312 + \frac{0.565}{p} - \frac{0.100}{p^2} \tag{5}$$

Example calculations of the surface coverage estimated assuming diffusion-limited adsorption to a planar surface are included in the Supporting Information.

4.6. Thermal imaging

The heating of the gradients under irradiation with an 808 nm laser (BWT Beijing Ltd., model DS3-51523-50.00 W) was evaluated using a testo 871 s thermal imager. Laser power output was measured using an optical power meter (PM-160 T HP, Thorlabs) and the laser beam spot size was determined using a laser detector card (VRC4, Thorlabs), details are available in the Supporting Information. The gradient samples were placed onto a glass coverslip that was suspended on a support stage with an opening beneath the sample, ensuring that only the gradient surface was exposed to NIR laser beam. The gradients were irradiated with an intensity of 0.6 W cm^{-2} and thermal images were captured during irradiation, after 10 s, 30 s, and 50 s.

4.7. X-ray diffraction

XRD patterns were collected on a SAXSLAB Mat:Nordic instrument equipped with a Rigaku 003 microfocusing Cu X-ray source producing a parallel beam from a two-bounce monochromator, and two Dectris detectors: Pilatus3 300 K R (orthogonal to the beam) and 100 K (on a goniometer circle centered at the sample position). Part of the beam path was evacuated during measurement to reduce air scattering and increase signal quality, while the sample was kept under dry nitrogen atmosphere during measurements. The incidence angle was set to around 22°, and the detector was positioned at 44° to maximize signal from the gold nanorods, which are oriented with reference to the substrate surface, as described in previously published work [22]. For *in situ* XRD, the NIR laser was equipped with a CFCS5-B adjustable fiber collimator from Thorlabs. Details on the power output and beam area of the laser setup used in the *in situ* XRD study are included in the Supporting Information. For these experiments we used a 0.15 mm min^{-1} gradient sample, and the laser collimator was placed directly above the sample at a distance of 15 mm. The size of the laser beam was approximately 2 mm in diameter, and the X-ray beam was set to 2 × 2 mm. A photo of the experimental setup is shown in Fig. S5. Irradiation experiments were performed at four positions along the gradient: 9, 12, 15 and 18 mm. At each position, XRD patterns were recorded at room temperature and under consecutive irradiation at 28, 56, 84, and 112 W cm^{-2}. Exposure times were adjusted to ensure adequate signal-to-noise ratio at each position along the gradient: 600 s at 9 mm, 420 s at 12 mm, 300 s at 15 mm, and 180 s at 18 mm. The acquired 2D images were processed using SAXSGUI software. Peak intensity and lattice

parameters were determined by fitting the (200) diffraction peak using TOPAS v6 (Bruker AXS).

Funding sources

Area of Advance in Materials Science at Chalmers University of Technology, Sweden. Knut and Alice Wallenberg Foundation through the Wallenberg Academy Fellow program.

CRediT authorship contribution statement

Maja Lidström Uusitalo: Writing – review & editing, Writing – original draft, Visualization, Methodology, Investigation, Formal analysis, Data curation, Conceptualization. **Michal Strach:** Writing – review & editing, Writing – original draft, Methodology, Investigation, Data curation, Conceptualization. **Mats Hulander:** Writing – review & editing, Conceptualization. **Martin Andersson:** Writing – review & editing, Supervision, Funding acquisition, Conceptualization.

Declaration of competing interest

The authors declare that they have no known competing financial interests or personal relationships that could have appeared to influence the work reported in this paper.

Appendix A. Supplementary data

Supplementary data to this article can be found online at https://doi.org/10.1016/j.apsusc.2026.166104

Data availability

Data will be made available on request.

References

[1] M.J. Ndolomingo, N. Bingwa, R. Meijboom, Review of supported metal nanoparticles: synthesis methodologies, advantages and application as catalysts, J. Mater. Sci. 55 (2020) 6195–6241, https://doi.org/10.1007/s10853-020-04415-x.

[2] K. Saha, S.S. Agasti, C. Kim, X. Li, V.M. Rotello, Gold nanoparticles in chemical and biological sensing, Chem. Rev. 112 (5) (2012) 2739–2779, https://doi.org/10.1021/cr2001178.

[3] M. Arnold, M. Schwieder, J. Blümmel, E.A. Cavalcanti-Adam, M. López-Garcia, H. Kessler, B. Geiger, J.P. Spatz, Cell interactions with hierarchically structured nano-patterned adhesive surfaces, Soft Matter 5 (1) (2009) 72–77, https://doi.org/10.1039/b815634d.

[4] D. Campoccia, L. Montanaro, C.R. Arciola, A review of the biomaterials technologies for infection-resistant surfaces, Biomaterials 34 (34) (2013) 8533–8554, https://doi.org/10.1016/j.biomaterials.2013.07.089.

[5] S. Kasani, K. Curtin, N. Wu, A review of 2D and 3D plasmonic nanostructure array patterns: fabrication, light management and sensing applications, Nanophotonics 8 (12) (2019) 2065–2089, https://doi.org/10.1515/nanoph-2019-0158.

[6] A.N. Shipway, E. Katz, I. Willner, Nanoparticle arrays on surfaces for electronic, optical, and sensor applications, ChemPhysChem 1 (1) (2000) 18–52.

[7] R. Borah, A.G. Karthick Raj, A.C. Minja, S.W. Verbruggen, A review on self-assembly of colloidal nanoparticles into clusters, patterns, and films: emerging synthesis techniques and applications, Small Methods (2023), https://doi.org/10.1002/smtd.202201536.

[8] R.R. Bhat, D.A. Fischer, J. Genzer, Fabricating planar nanoparticle assemblies with number density gradients, Langmuir 18 (15) (2002) 5640–5643, https://doi.org/10.1021/la025524m.

[9] R.V. Goreham, R.D. Short, K. Vasilev, Method for the generation of surface-bound nanoparticle density gradients, J. Phys. Chem. C 115 (8) (2011) 3429–3433, https://doi.org/10.1021/jp111221g.

[10] A. Lundgren, S. Munktell, M. Lacey, M. Berglin, F. Björefors, Formation of gold nanoparticle size and density gradients via bipolar electrochemistry, ChemElectroChem 3 (3) (2016) 378–382, https://doi.org/10.1002/celc.201500413.

[11] T.A. Kumar, A. Bardea, Y. Shai, A. Yoffe, R. Naaman, Patterning gradient properties from sub-micrometers to millimeters by magnetolithography, Nano Lett. 10 (6) (2010) 2262–2267, https://doi.org/10.1021/nl1013635.

[12] A. Lundgren, M. Hulander, J. Brorsson, M. Hermansson, H. Elwing, O. Andersson, B. Liedberg, M. Berglin, Gold-nanoparticle-assisted self-assembly of chemical gradients with tunable sub-50 Nm molecular domains, Part. Part. Syst. Char. 31 (2) (2014) 209–218, https://doi.org/10.1002/ppsc.201300154.

[13] C. Huwiler, T.P. Kunzler, M. Textor, J. Vörös, N.D. Spencer, Functionalizable nanomorphology gradients via colloidal self-assembly, Langmuir 23 (11) (2007) 5929–5935, https://doi.org/10.1021/la0700422.

[14] P.K. Jain, X. Huang, I.H. El-Sayed, M.A. El-Sayed, Noble Metals on the nanoscale: optical and photothermal properties and some applications in imaging, sensing, biology, and medicine, Acc. Chem. Res. 41 (12) (2008) 1578–1586, https://doi.org/10.1021/ar7002804.

[15] O. Bar-Ilan, R.M. Albrecht, V.E. Fako, D.Y. Furgeson, Toxicity assessments of multisized gold and silver nanoparticles in zebrafish embryos, Small 5 (16) (2009) 1897–1910, https://doi.org/10.1002/smll.200801716.

[16] E.E. Connor, J. Mwamuka, A. Gole, C.J. Murphy, M.D. Wyatt, Gold nanoparticles are taken up by human cells but do not cause acute cytotoxicity, Small 1 (3) (2005) 325–327, https://doi.org/10.1002/smll.200400093.

[17] P.V. Asharani, Y. Lianwu, Z. Gong, S. Valiyaveettil, Comparison of the toxicity of silver, gold and platinum nanoparticles in developing zebrafish embryos, Nanotoxicology 5 (1) (2011) 43–54, https://doi.org/10.3109/17435390.2010.489207.

[18] R. Weissleder, A clearer vision for *in vivo* imaging, Nat. Biotechnol. 19 (2001) 316–317.

[19] A.M. Funston, C. Novo, T.J. Davis, P. Mulvaney, Plasmon coupling of gold nanorods at short distances and in different geometries, Nano Lett. 9 (4) (2009) 1651–1658, https://doi.org/10.1021/nl900034v.

[20] A.S. Dimitrov, K. Nagayama, Continuous convective assembling of fine particles into two-dimensional arrays on solid surfaces, Langmuir 12 (5) (1996) 1303–1311.

[21] J. Mosquera, D. Wang, S. Bals, L.M. Liz-Marzán, Surfactant layers on gold nanorods, Acc. Chem. Res. 56 (10) (2023) 1204–1212, https://doi.org/10.1021/acs.accounts.3c00101.

[22] M. Uusitalo, M. Strach, G. Eriksson, T. Dmytrenko, J. Andersson, A. Dahlin, M. Hulander, M. Andersson, Photothermal properties of solid-supported gold nanorods, Nano Lett. 24 (40) (2024) 12529–12535, https://doi.org/10.1021/acs.nanolett.4c03472.

[23] G. Baffou, P. Berto, E. Bermúdez Ureña, R. Quidant, S. Monneret, J. Polleux, H. Rigneault, Photoinduced heating of nanoparticle arrays, ACS Nano 7 (8) (2013) 6478–6488, https://doi.org/10.1021/nn401924n.

[24] M. Uusitalo, G. Eriksson, M. Hulander, M. Andersson, Gold nanorods as photothermal antibacterial materials, ACS Appl. Nano Mater. 8 (7) (2025) 3661–3670, https://doi.org/10.1021/acsanm.5c00324.

[25] L. Scarabelli, A. Sánchez-Iglesias, J. Pérez-Juste, L.M. Liz-Marzán, A "tips and tricks" practical guide to the synthesis of gold nanorods, J. Phys. Chem. Lett. 6 (21) (2015) 4270–4279, https://doi.org/10.1021/acs.jpclett.5b02123.

[26] Z. Adamczyk. Particles at Interfaces: Interactions, Deposition, Structure, 1st ed.; Adamczyk, Z., Ed.; Academic Press: Amsterdam, 2006; Vol. 9.

[27] M. Mercedes Tirado, C. López Martínez, J. García De La Torre, Comparison of theories for the translational and rotational diffusion coefficients of rod-like macromolecules. application to short DNA fragments, J. Chem. Phys. 81 (1984) 2047–2052, https://doi.org/10.1063/1.447827.